Effective role of mineral oil and biological nanomaterial on thermal energy influenced by magnetic dipole and nanoparticle shape

Umar Nazir[1], Muhammad Sohail[2]*, Samaira Naz[3], Kanit Mukdasai[1], Manoj Singh[4], Abha Singh[5], Chandika Rama Mohan[6], Sayed M. Eldin[7]* and Ahmed M. Galal[8,9]

[1]Department of Mathematics, Faculty of Science, Khon Kaen University, Khon Kaen, Thailand, [2]Institute of Mathematics, Khwaja Fareed University of Engineering and Information Technology, Rahim Yar Khan, Pakistan, [3]Department of Mathematics, Government College University Faisalabad, Faisalabad, Pakistan, [4]Department of Mathematics, Faculty of Science, Jazan University, Jazan, Saudi Arabia, [5]Department of Basic Sciences, College of Sciences and Theoretical Studies, Dammam-Branch, Saudi Electronic University, Riyad, Saudi Arabia, [6]Clinical Nutrition Department Applied Medical Science College Jazan University, Jazan, Saudi Arabia, [7]Center of Research, Faculty of Engineering, Future University in Egypt, New Cairo, Egypt, [8]Mechanical Engineering Department, College of Engineering, Prince Sattam Bin Abdulaziz University, Al-Kharj, Saudi Arabia, [9]Production Engineering and Mechanical Design Department, Faculty of Engineering, Mansoura University, Mansoura, Egypt

This study of synovial fluid was conducted by considering two different nanofluid models over a two-dimensional stretched surface using nanoparticles of different shapes. We obtained remarkable results regarding the impact of nanoparticles on thermal performance. Through this study, we assessed heat and mass transfer and the involvement of magnetic dipole of chemically reactive species in two-dimensional steady incompressible flow. Heat generation was incorporated in the energy equation and a first-order chemical reaction was involved in the mass transport phenomenon. The concept of boundary layer was adopted to derive the physical problem in Cartesian coordinates, with results in the form of coupled partial differential equations (PDEs). The derived PDEs were highly non-linear, and exact solutions were not possible. Therefore, the PDEs were converted into non-linear ordinary differential equations (ODEs) using appropriate similarity transformation and then solved numerically *via* the finite element method. The impact of numerous emerging parameters on the solutions are displayed graphically, and the physical significance is discussed. An increment in Sc, K_c, and γ decelerated the solute field, while the concentration gradient increased with enhancement in Sc. Maximum acceleration in velocity for model-I was produced compared to acceleration in the velocity field for model-II.

KEYWORDS

nanomaterial shape, biological fluid, heat source, nanoparticles, magnetic dipole, thermo-phoretic particle, flat plate

1 Introduction

In laboratories worldwide, researchers are investigating a wide range of possible applications for nanofluids. These applications include mineral oils, water, solar energy, and microelectronics. It is possible that using chemotherapy in conjunction with nanoparticles will result in the death of cancer cells. The operation of the thermal extrusion mechanism is not due to the presence of low-energy reservoirs but rather to the process by which nanoparticles are produced. Thermo-physical

properties of nano-liquids, such as thermal infusibility and thermal conductivity, are among the most advanced in the industry, which could benefit various industries. It is possible to use nanomaterials in multiple applications, such as cooling of engines, processing of pharmaceuticals, operation of fuel cells, and function of residential cooling systems. Large-capacity cooling systems are now feasible thanks to the energy-saving characteristics of nano-liquids. A nano liquid-based smart material has the potential to regulate the flow of heat and act as a heat valve. In addition to these applications, there are potential uses of nano-liquids in geothermal energy production and fuel production for nuclear reactors. Both the minimum quantity cooling lubrication (MQCL) and the MQCG nanofluid technologies benefit the environment due to their reduced reliance on oil and grease. They not only cool and lubricate but also eliminate the need for cutting fluids. Choi and Eastman (1995) developed the concept of nanofluids. Nanofluids are characterized by nanoparticles suspended in liquids. The behavior of a nano-liquid can be significantly altered depending on the temperature and viscosity of the fluid's boundary layer. Khan et al. (2021a) discussed the role of gold nanoparticles in Sisko fluid under the impacts of thermal radiation and Lorentz force using slip conditions toward a curved surface. Khan et al. (2021b) derived mono and hybrid nanomaterials in motion at the stagnation point utilizing characteristics of the microstructure of moveable frames *via* non-isothermal condition. Khan et al. (2022a) studied various impacts of stagnation point characteristics in thermal and mass diffusion fields under the role of magnetic fields containing graphene oxide and water nanoparticles on the surface. Khan et al. (2022b) have driven multiple features of AA7075 and AA7072 nanoparticles within heat transfer on a cylinder utilizing slip conditions. Akbar et al. (2022) described the heat transfer mechanism of unsteady peristaltic liquid, including variable thermal properties, *via* the exact solution approach. Akram et al. (2022a) modeled the flow of peristaltic propulsion in the motion of TiO$_2$/10W40 nanoparticles using mechanisms of electro-osmotics in a curved microchannel. Maraj et al. (2017) estimated the consequences of Lorentz force and thermal deposition in a vertical channel filled with carbon nanotubule (CNT) nanoparticles. Akram et al. (2022b) modeled a flow problem based on peristaltic transport that involved adding a mixture of nanoparticles considering Lorentz force in aqueous media. Shafee et al. (2021) developed a non-equilibrium theory that sheds light on how the shape factor, Lorentz force, and radiation term influence heat transfer and behavior in nanomaterials. Akbar et al. (2019) analyzed features of ethylene glycol in thermal transfer when inserting suspensions of different shaped nanoparticles in a vertical channel. Habib and Akbar (2021) investigated the use of dispersed nanoparticles to combat *Staphylococcus aureus* in clinical isolates.

When electrokinetic Jeffrey fluid and peristalsis are combined, a phenomenon known as the Soret–Dufour cross-diffusion effect occurs. When scientists are trying to figure out how streamlines move, they frequently consider the "trapping theory" as one of the possible explanations. Peristalsis is defined as a wave-like movement of fluids through a channel, which happens naturally in the body. The production of heat is caused by the passage of a chemically reactive liquid through a porous medium with the assistance of a semi-infinite vertical permeable plate, which also contributes to the movement of the liquid. Hall currents and a liquid called Jeffrey liquid have been studied by Babu et al. (2020). Ali et al. (2020) researched how heat and thermal energy moved through the stretching cylinder in Jeffrey fluids. During an experiment conducted by Aleem and Alex, there was a consistent flow of Jeffrey fluid between two hot plates. The existence of a strong magnetic field piqued their

interest in this subject matter. According to Saif et al. (2020), the mechanisms that control the flow of magnetic hydrodynamic (MHD) fluid and heat transfer are governed by the curvature of the stretching surface. Research conducted by Gireesha et al. (2020) looked at the three-dimensional flow of radiating Jeffrey liquids on a stretched surface. According to Manjunatha et al. (2020), the effects of heat and solutes on peristaltic flow of Jeffrey fluid are not uniformly distributed throughout the system. This plan defies logic in every way. Sinha et al. (2020) investigated the effects of thermal radiation and Hall current on a nanofluid. Use of a thermal tube that vibrated and emitted moving ultrasound waves was required for that method. The effect of a specific variable electrical field on the flow of Jeffrey fluid is illustrated in Haroun (2020). As part of their experiment, they observed the non-steady and hydromagnetic flow using a flat plate and a magnetic field to observe the flow of the electrical conductor but incompressible fluid. In a porous Darcy-type medium, a third-grade nano-liquid that is optically dense and electrically conductive transfers heat to a porous surface *via* a Lie symmetry mechanism. This surface is located in the middle of the medium. This nano-liquid has a high density when measured in light and electricity. Maraj et al. (2022) discussed the results of rotational flow in a channel filled with hybrid nanoparticles under the impact of Lorentz forces using slip conditions. Akram et al. (2021) estimated theoretical results of thermal transfer with a mixture of hybrid nanoparticles and base fluid (water) in microchannels *via* electroosmotic pumping.

Bioconvection makes the growth process easier for bacteria and algae suspended in water. Microorganisms make the process of bioconvection possible. Microbes capable of bioconvection rise to the surface because they are 5–10 percent denser than water. They are referred to as "bioconvective" because of this characteristic. The action of these microorganisms causes the primary fluid to become thicker as a side effect. Examples of bioconvection can be observed in a wide variety of organic applications and microsystems, pharmaceuticals, biopolymers, environmentally friendly applications, developments in the utilization of cost-effective energy sources, microbial advanced oil recovery, biosensors and biotechnology, and continuous numerical display. One industry that uses bioconvection is the continuous numerical display (CND) industry. In their analysis, they examined MHD flow of nanofluids in the vicinity of a stretching surface, taking both velocity slip and viscous dissipation into account; in their research on the ferromagnetic materials of general Newtonian fluids, Khan et al. used bioconvection species that were chemically and paraboloid reactive. For example, Shehzad et al. (2020) have demonstrated that fluid can flow through spinning discs, analogous to the way water flows through tubes. Khan et al. (2020) proposed the hypothesis that gyrotactic microorganisms move around in nano-liquids that have thixotropic viscosity. According to Veera Krishna (2020), a magnetic field is generated when a steady convective magnetohydrodynamic flow of a viscous nanofluid is combined with a permeable porous surface that expands exponentially. As a consequence of the interaction of these two variables, the magnetic field will exhibit some movement. The Carreau–Yasuda nanofluid flow was the result of combining the findings of Hassan et al. (Waqas et al., 2020) on second-order velocity slip and moving microorganisms. Akram et al. (2022c) analyzed electroosmotic flow based on peristalsis flow of silver–water nanomaterials by implementing two approaches. Research conducted by Hosseinzadeh et al. (2020) focused on second-grade convective nanofluid flows. A square cavity that was open on all sides was used to investigate how an oxytactic microbe moved throughout the space. The Boussinesq–Darcy approximation was utilized for both the flow of
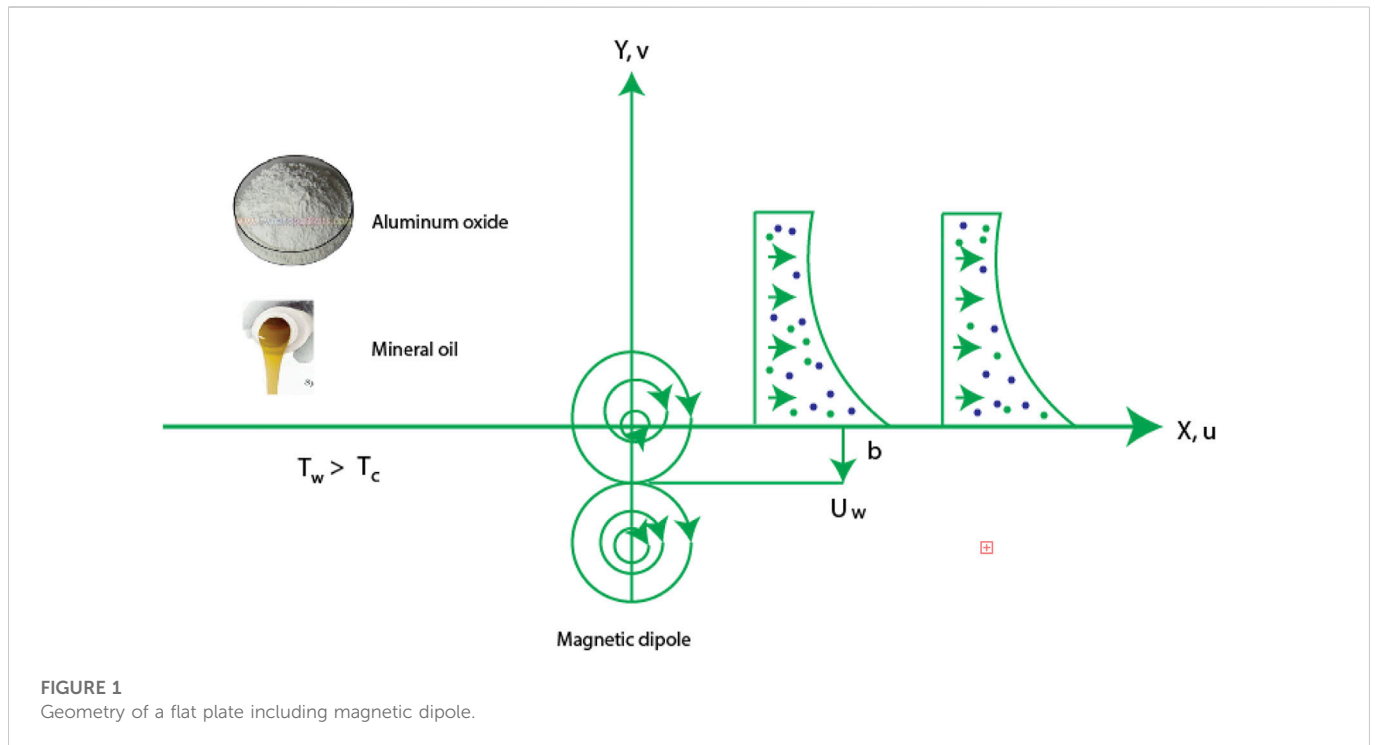
FIGURE 1
Geometry of a flat plate including magnetic dipole.

TABLE 1 Thermal properties associated with nanoparticles in base liquid (Hanif and Shafie, 2022; Wang et al., 2022).

	ρ	K	C_p	σ	μ
Al_2O_3	3,970	40		765	35×10^6
Mineral oil	861	0.157	1860	$0.33 \ 10^{-9}$	0.01335

heat and bioconvection. Activation energy and gyrotactic microorganisms are being used to study nanofluid rheology throughout porous media. A horizontal porous expansion sheet can influence the flow of a fluid infested with gyrotactic microorganisms in a manner comparable to that of a magnetohydrodynamic model for students using the third-grade model (Madhukesh et al., 2022).

Rostami et al. (2022) studied the hydro-thermal analysis. Moreover, the studies reported by, Hosseinzadeh et al. (2021a); Hosseinzadeh et al. (2021b); Sohail et al. (2022a); Sohail et al. (2022b); Hou et al. (2022) are prepared to notice the comportment of numerous involved parameters on momentum and thermal transport. There are no studies in the existing literature that involve synovial fluid and consider the two different nanofluid models over a two-dimensional stretched surface through use of different shaped nanoparticles. In the current study, the modeled problem is solved numerically, and the results are displayed through tables and graphs.

2 Model characteristics and mathematical analysis

The following assumptions were made:

➢ SF (synovial fluid) is considered over a 2D surface;
➢ Several shapes (cylinder, brick, sphere, and platelet) of nanoparticles are addressed;

➢ Magnetic dipole is considered;
➢ Correlations based on nanoparticles are assumed;
➢ Heat source is taken out;
➢ Chemical species and thermo-phoretic properties are addressed;
➢ Base fluid is taken as mineral oil;
➢ Figure 1 represents the geometry of the model.

Two models of viscosity (Salmi et al., 2022) are defined as

$$\mu(C, N) = e^{bC}\mu_0 \left(\gamma^2|N|^2 + \varepsilon\right)^n \text{ for model} - \text{I.} \qquad (1)$$

$$\mu(C, N) = \mu_0 \left(\gamma^2|N|^2 + \varepsilon\right)^{n(c)} \text{ for model} - \text{II.} \qquad (2)$$

Here, Eqs 1, 2 are known as model-I and model II, respectively. Governing equations (Salmi et al., 2022; Wang et al., 2022) are derived utilizing conservation laws. PDEs in view of SF implicating magnetic dipole are

$$u_X + v_Y = 0, \qquad (3)$$

Two models regarding momentum equations are obtained using Eqs (1) and (2). Momentum equation for model-I is

$$\rho_{Nf}(uu_X + vu_Y) = -P_x + M\mu_{Nf}H_x$$
$$+2\mu_{Nf}\left[\begin{array}{l} u_{YY} + 3n\gamma^2(u_Y)^2 u_{YY} + \alpha^\star u_{YY}\phi + \alpha^\star u_Y \phi_Y \\ +\alpha^\star n\gamma^2(u_Y)^3\phi_Y + 3\alpha^\star n\gamma^2\phi(u_Y)^2 u_{YY} \end{array} \right], \qquad (4)$$

The momentum equation for model-II is

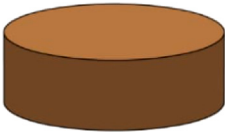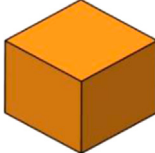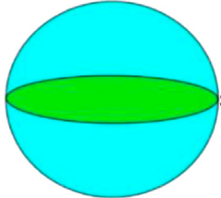**TABLE 2 Shapes of nanoparticles associated with size (Naseem et al., 2021).**

Shape of nanoparticles	M	A_1	A_2
Platelet	5.72	37.1	612.6
Cylinder	4.82	13.5	904.4
Brick	3.72	1.9	471.4
Sphere	3.0	2.5	6.5

TABLE 3 Grid size analysis in terms of velocity, concentration, and temperature fields simulated by 300 elements when $\alpha = 2.0, n = 0.5, Re = 2.0, \gamma = 3.0, \beta = 1.3,$
$\Lambda = 0.3, Pr = 5.0, \epsilon = 0.1, H_t = 2.0, Sc = 0.4, \lambda = 0.4, K_c = -1.5, \chi = 0.3, \tau = 0.3,$ **and** $We = 0.7.$

e	$F'\left(\frac{\eta_\infty}{2}\right)$	$\theta\left(\frac{\eta_\infty}{2}\right)$	$\phi\left(\frac{\eta_\infty}{2}\right)$
30	0.5333,333,270	0.1754,080,591	0.3094,245,544
60	0.5166,666,704	0.1648,496,296	0.2950,440,665
90	0.5111,110,865	0.1614,464,769	0.2903,546,386
120	0.5083,333,305	0.1597,661,853	0.2880,288,454
150	0.5066,666,515	0.1587,644,986	0.2866,390,692
180	0.5055,555,689	0.1580,996,219	0.2857,156,200
210	0.5047,636,551	0.1576,259,302	0.2850,569,932
240	0.5041,665,982	0.1572,718,391	0.2845,632,498
270	0.5037,037,880	0.1569,962,944	0.2841,804,318
300	0.5033,309,189	0.1567,760,666	0.2838,742,789

$$\rho_{Nf}\left(uu_X + vu_Y\right) = -P_x + M\mu_{Nf}H_x$$
$$+ 2\mu_{Nf}\left[u_{YY} - \frac{\alpha^\star \gamma^2}{2}(u_Y)^3\phi_Y - \frac{3\alpha^\star \gamma^2}{2}\phi(u_Y)^2 u_{YY}\right],$$
$$(5)$$

$$(uT_X + vT_Y) + \frac{1}{\left(\rho C_P\right)_{Nf}}\left(uH_x + vH_Y\right)\mu_{Nf}TM_T$$

$$= \frac{K_{Nf}}{\left(\rho C_P\right)_{Nf}}T_{yy} - \frac{Q_0}{\left(\rho C_P\right)_{Nf}}\left(T - T_\infty\right), \quad (6)$$

The mass diffusion equation (Madhukesh et al., 2022) is defined as

$$uC_X + vC_Y = DT_{yy} + \left(\left(C - C_\infty\right)k_{\gamma_f}\frac{T_w - T_\infty}{T_s}\right)_y - K\left(C - C_\infty\right). \quad (7)$$

Developing boundary conditions (Wang et al., 2022) are

$$C = C_w, v = 0, u = U_w = aX, T = T_w: \ y = 0,$$
$$T \to T_\infty = T_c, u \to u_e, C \to C_\infty: \ y \to \infty. \quad (8)$$

The magnetic field *via* magnetic dipole (Wang et al., 2022) is

$$\beta_1 = \frac{\delta}{2\pi}\left(\frac{X}{X^2 + (Y + d)^2}\right). \quad (9)$$

TABLE 4 Validation results for Nusselt number based on published data (Muhammad and Nadeem, 2017)
when $H_t = 0, \beta = \epsilon = 0 = \Lambda = 0, \chi = 0, \lambda = 0, \alpha = 0.3, n = 0.2, Re = 3.0, We = 2.0, Sc = 0.4, K_c = -1.5,$ and $\tau = 0.3$.

Pr	Present results	Muhammad and Nadeem (2017)
0.72	0.8086,330,926	0.808,641
1.0	1.0005,315,382	1.000000
3.0	1.9232,636,052	1.923,690
4.0	2.0031,160,400	2.003170

FIGURE 2
Effect of *We* on velocity curves when $\alpha = 0.4, n = 0.2, Re = 2.0, \gamma = 0.2, \beta = 1.3, \Lambda = 0.32, Pr = 5, \epsilon = 0.1, H_t = -1.6, Sc = 0.4, \lambda = 0.4, K_c = -1.5, \chi = 0.3,$ and $\tau = 0.3$.

FIGURE 3
Effect of H_t on velocity curves when $\alpha = 0.3, n = 0.2, Re = 3.0, We = 2.0, \gamma = 0.2, \beta = 1.7, \Lambda = 0.3, Pr = 3, \epsilon = 0.4, Sc = 0.4, \lambda = 0.4, K_c = -1.5, \chi = 0.5,$ and $\tau = 0.3$.
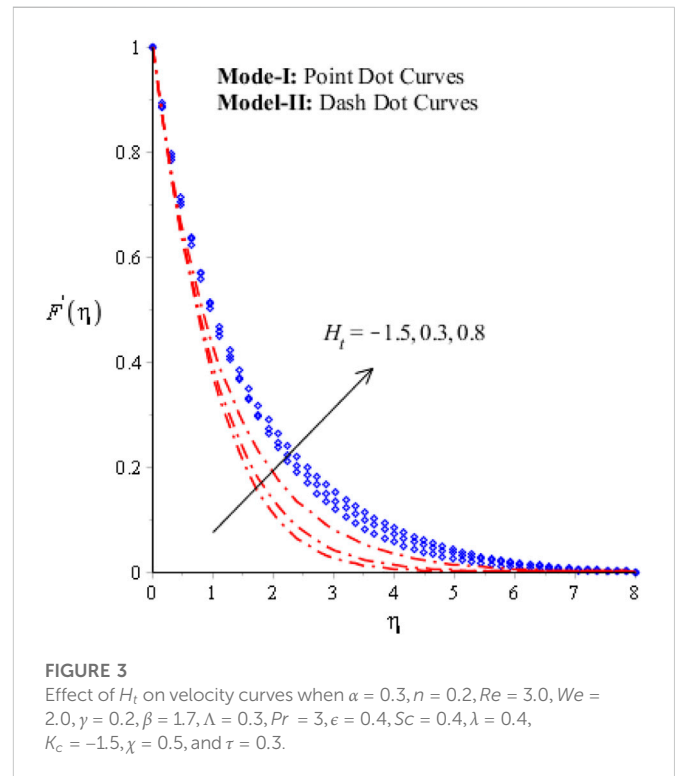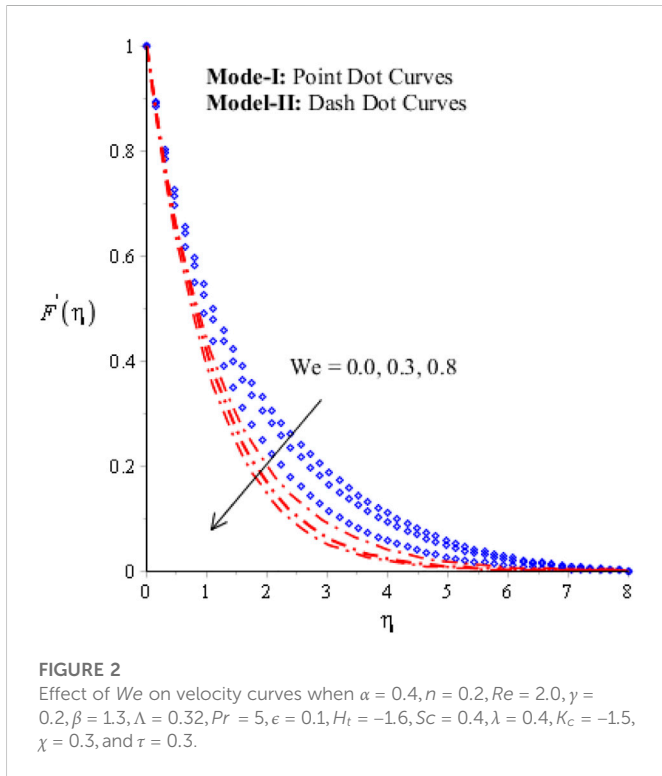
Components of magnetic dipole (Wang et al., 2022) are

$$H_X = -\frac{\partial \delta}{\partial X} = \frac{\delta}{2\pi}\left(\frac{X^2 - (Y+d)^2}{\{X^2 + (Y+d)^2\}^2}\right), \quad (10)$$

$$H_Y = -\frac{\partial \delta}{\partial Y} = \frac{\delta}{2\pi}\left(\frac{2X(Y+d)}{\{X^2 + (Y+d)^2\}^2}\right). \quad (11)$$

The magnitude of magnetic dipole (Wang et al., 2022) is

$$H = \left(\left(\frac{\partial \delta}{\partial Y}\right)^2 + \left(\frac{\partial \delta}{\partial X}\right)^2\right)^{\frac{1}{2}}, \quad (12)$$

$$\frac{\partial H}{\partial Y} = \frac{\delta}{2\pi}\left[-\frac{2}{(Y+d)^3} + \frac{4X^2}{(Y+d)^5}\right], \frac{\partial H}{\partial X} = -\frac{\delta}{2\pi}\left[-\frac{2X}{(Y+d)^4}\right], \quad (13)$$

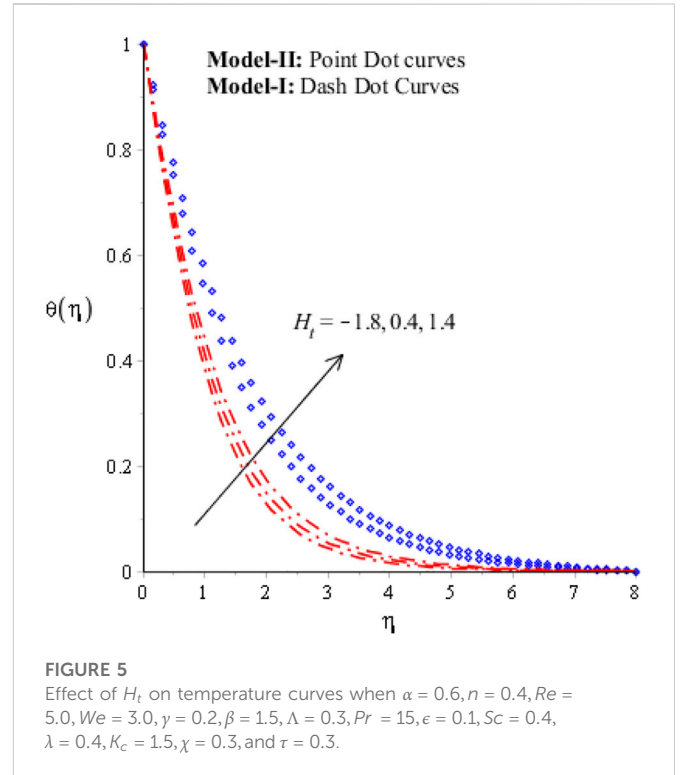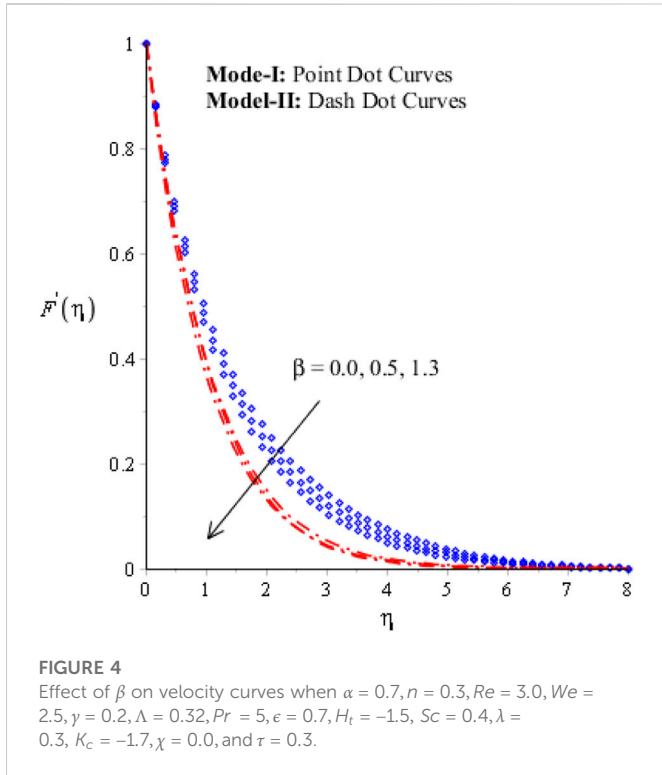Similarity variables (Gul et al., 2020; Wang et al., 2022) are defined as

$$u = aXF', v = -\left(av_f\right)^{\frac{1}{2}}F, \theta = \frac{T_c - T}{T_c - T_w}, \eta = X\left(\frac{a\rho_f}{\mu_f}\right)^{\frac{1}{2}}, \phi = \frac{C_\infty - C}{C_\infty - C_w}. \quad (14)$$

Dimensionless representations of ODEs (Gul et al., 2020; Salmi et al., 2022; Wang et al., 2022) are

$$2\left[\left(1 + \alpha\phi + nReWe^2F'^2 + 3nReWe^2F'^2\phi\right)F'''\right] + 2n\alpha\gamma^2F''\phi] + 2n\gamma^2F''\phi,$$

$$+2nReWe^2F'^3\phi' - \frac{v_{Nf}}{v_f}\left[F'F' + FF'' - \frac{\theta 2\beta}{(\eta+\Lambda)^4}\right] = 0, \quad (15)$$

$$2\left[\left(1 - 3\alpha ReWe^2F'^2\phi\right)F'''\right] - \alpha ReWe^2F'^3\phi'$$

$$-\frac{v_{Nf}}{v_f}\left[F'F' + FF'' - \frac{\theta 2\beta}{(\eta+\Lambda)^4}\right] = 0, \quad (16)$$

$$\theta'' + \frac{(\rho C_p)_{Nf}k_f}{(\rho C_p)_f k_{Nf}}Pr\left(F\theta' - 2F'\theta\right) + \frac{(\rho C_p)_{Nf}k_f}{(\rho C_p)_f k_{Nf}}\frac{\lambda 2\beta f\left(\theta - \epsilon\right)}{(\eta+\Lambda)^3}$$

$$+\frac{k_f}{k_{Nf}}PrH_t\theta = 0, \quad (17)$$

FIGURE 4
Effect of β on velocity curves when $\alpha = 0.7, n = 0.3, Re = 3.0, We = 2.5, \gamma = 0.2, \Lambda = 0.32, Pr = 5, \epsilon = 0.7, H_t = -1.5, Sc = 0.4, \lambda = 0.3, K_c = -1.7, \chi = 0.0,$ and $\tau = 0.3$.

FIGURE 5
Effect of H_t on temperature curves when $\alpha = 0.6, n = 0.4, Re = 5.0, We = 3.0, \gamma = 0.2, \beta = 1.5, \Lambda = 0.3, Pr = 15, \epsilon = 0.1, Sc = 0.4, \lambda = 0.4, K_c = 1.5, \chi = 0.3,$ and $\tau = 0.3$.

$$(1 - \chi)^{2.5} \phi'' + ScF\phi' + \frac{\lambda 2 \beta f (\phi - \epsilon)}{(\eta + \Lambda)^3} - \tau Sc\theta'' \phi + \theta' \phi' + K_c Sc\phi = 0. \tag{18}$$

Correlations based on nanoparticles were captured as indicated as follows. The nanoparticle properties are listed in Table 1 and Table 2 contains information about nanoparticle shapes (Naseem et al., 2021).

$$K_{Nf} = \frac{-2\chi(-K_s + K_f) + 2K_f + K_s}{2\chi(-K_s + K_f) + 2K_f + K_s}, \mu_{Nf} = \frac{\mu_f}{(1 - \chi)^{2.5}}, \rho_{Nf}$$

$$= \rho_f \left(1 - \chi + \chi \frac{\rho_s}{\rho_f} \right), \tag{19}$$

$$D_{Nf} = D_f (1 - \chi)^{2.5}, (\rho C_P)_{Nf} = \left(-\chi + 1 + \frac{(\rho C_P)_s}{(\rho C_P)_f} \chi \right) (\rho C_P)_f, \tag{20}$$
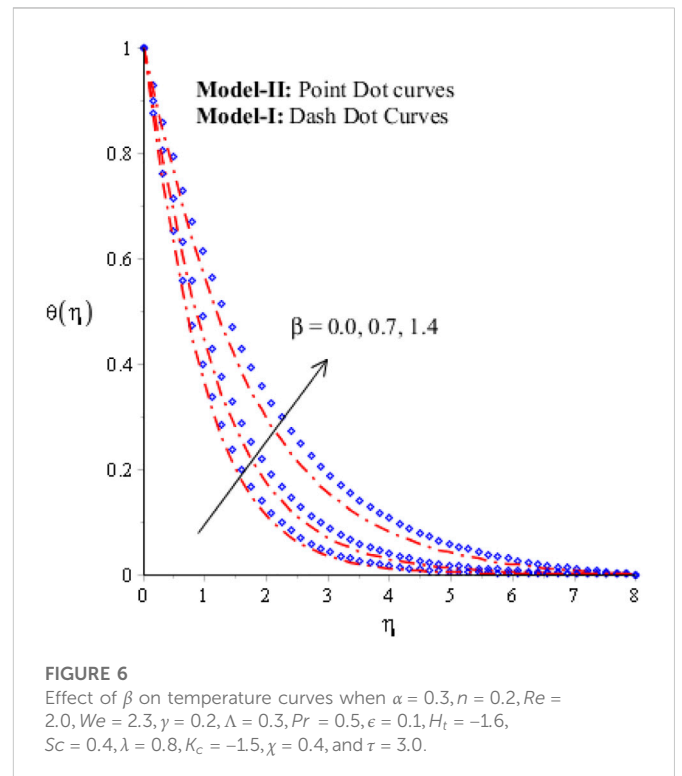
$$\frac{K_{Nf}}{K_f} = \frac{K_s + (m-1)K_f + (m-1)(K_s - K_f)\chi}{K_s + (m-1)K_f + (K_s - K_f)\chi}. \tag{21}$$

Boundary conditions (BCs) are

$$F(\eta) = 0, \theta(\eta) = 1, \phi(\eta) = 1, F'(\eta) = 1: \eta$$
$$= 0, F'(\eta) \to 0, \theta(\eta) \to 0, \phi(\eta) \to 0: \eta \to 0. \tag{22}$$

Parameters are defined as

$$Re = \frac{ax^2}{\nu_f}, We = \alpha\gamma^2, \beta = \frac{\delta}{2\pi} \frac{\mu_0 k(T_c - T_w)\rho_f}{(\mu_f)^2}, H_t = \frac{Q_0}{(C_P)_f a},$$

$$Pr = \frac{\mu C_P}{k}, K_c, Sc = \frac{\nu_f}{D_f},$$

$$\Lambda = \left(\frac{a(\mu_f)^2}{\rho_f k(T_c - T_w)} \right)^{1/2}, \tau = \frac{k_f (T_w - T_\infty)}{T_s}, \epsilon = \frac{T_\infty}{T_c - T_\infty}, K_c = \frac{K_c}{a},$$

$$\alpha = \alpha^* (C - C_\infty).$$

FIGURE 6
Effect of β on temperature curves when $\alpha = 0.3, n = 0.2, Re = 2.0, We = 2.3, \gamma = 0.2, \Lambda = 0.3, Pr = 0.5, \epsilon = 0.1, H_t = -1.6, Sc = 0.4, \lambda = 0.8, K_c = -1.5, \chi = 0.4,$ and $\tau = 3.0$.

Surface forces for model-I and model-II (Salmi et al., 2022) were delivered as

$$Re^{1/2}Cf = \frac{1}{(1 - \chi)^{2.5}} \left[(1 + \alpha\phi(0)F'') + RenWe^2 (1 + \alpha\phi(0))F'''(0)^3 \right], \tag{23}$$
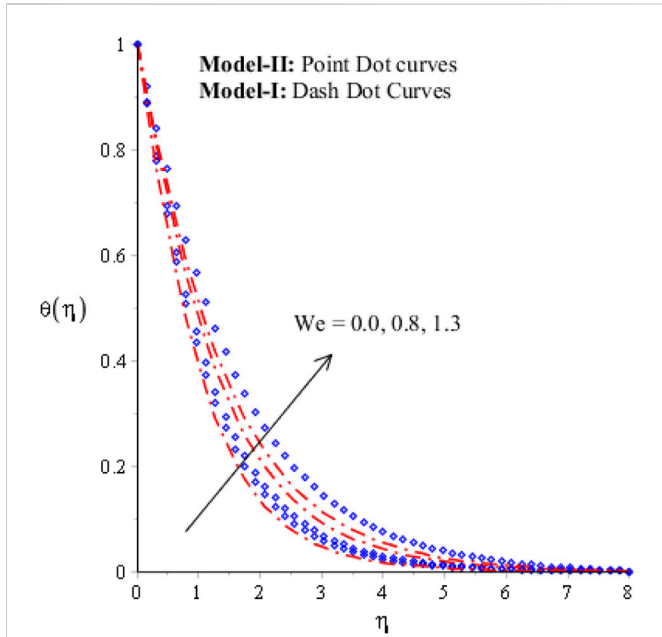
FIGURE 7
Effect of We on temperature curves when $\alpha = 0.4, n = 0.3, Re = 3.0, \gamma = 0.5, \beta = 1.3, \Lambda = 0.32, Pr = 5, \epsilon = 0.7, H_t = -1.6, Sc = 0.4, \lambda = 0.4, K_c = -1.7, \chi = 0.3,$ and $\tau = 0.3$.
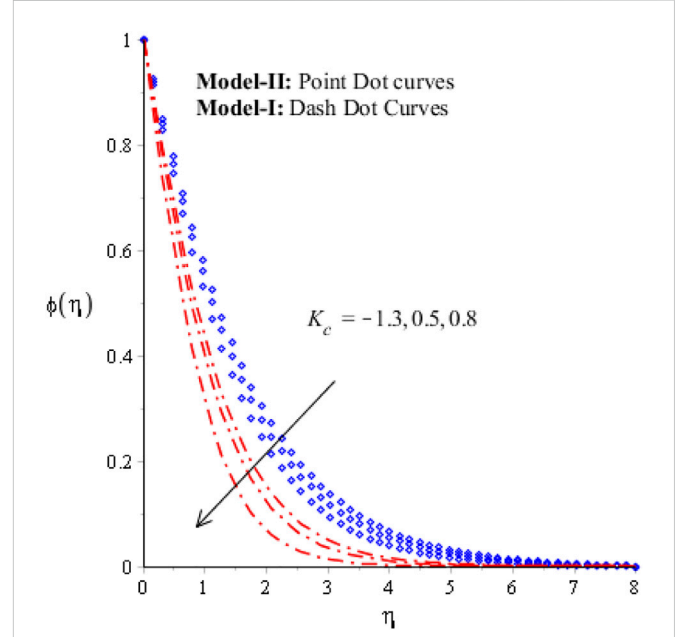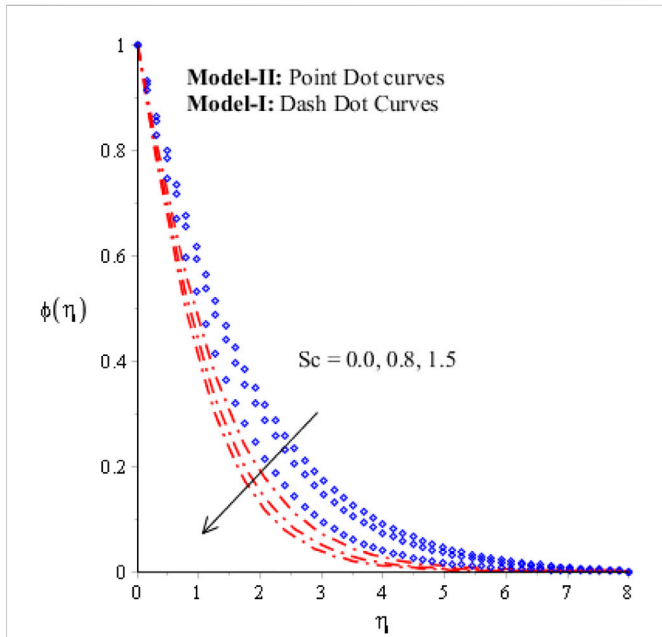

FIGURE 9
Effect of K_c on concentration curves when $\alpha = 2.0, n = 0.3, Re = 2.0, We = 5.0, \gamma = 0.4, \beta = 1.3, \Lambda = 0.2, Pr = 5, \epsilon = 0.8, H_t = -2.0, Sc = 0.4, \lambda = 0.3, \chi = 0.35,$ and $\tau = 0.8$.

$$Re^{-1/2}NU = -\frac{K_{Nf}}{K_f}\theta'(0), \quad Re^{-\frac{1}{2}}Sh = \frac{1}{(1-\chi)^{2.5}}\phi'(0). \quad (25)$$

3 Finite element analysis

The finite element method (FEM) was utilized to simulate numerical solution of ODE-associated BCs. Steps for explanation of the FEM are listed as follows.

Step-I: In step-I, the desired domain of the problem was discretized into a number of elements. Weak form was achieved using the concept of weighted residual. Shape functions based on linear-type polynomial were derived as follows.

The variables $N, F, \theta,$ and ϕ are defined as

$$N = \sum_{j=1}^{2}\left(N_j\psi_j\right), F = \sum_{j=1}^{2}\left(F_j\psi_j\right), \theta = \sum_{j=1}^{2}\left(\theta_j\psi_j\right), \phi = \sum_{j=1}^{2}\left(\phi_j\psi_j\right). \quad (26)$$

The shape function is

$$\psi_j = (-1)^{j-1}\frac{\eta - \eta_{j-1}}{\eta_j - \eta_{j-1}}. \quad (27)$$

Step-II: Stiffness elements were calculated over each element based on the breakdown of the problem domain. Moreover, a global stiffness matrix was achieved. The Picard approach was implemented to differentiate linear systems from non-linear systems. The residual view is defined as

$$[R] = \left[M\left(F^{(r-1)}, N^{(r-1)}, \theta^{(r-1)}, \phi^{(r-1)}\right)\right]\begin{bmatrix} F^r \\ \theta^r \\ \phi^r \end{bmatrix} = [F]. \quad (28)$$

FIGURE 8
Effect of Sc on concentration curves when $\alpha = 0.4, n = 0.2, Re = 3.0, We = 2.5, \gamma = 0.2, \beta = 1.3, \Lambda = 0.3, Pr = 5, \epsilon = 0.01, H_t = -1.6, \lambda = 0.4, \gamma = 0.4, K_c = -1.5, \chi = 0.3,$ and $\tau = 0.5$.

$$Re^{\frac{1}{2}}Cf = \frac{1}{(1-\chi)^{2.5}}\left[F''(0) + \frac{\alpha}{2}We^2ReF'''(0)^3\right]. \quad (24)$$

Temperature and concentration gradients for biological fluid (Salmi et al., 2022) are
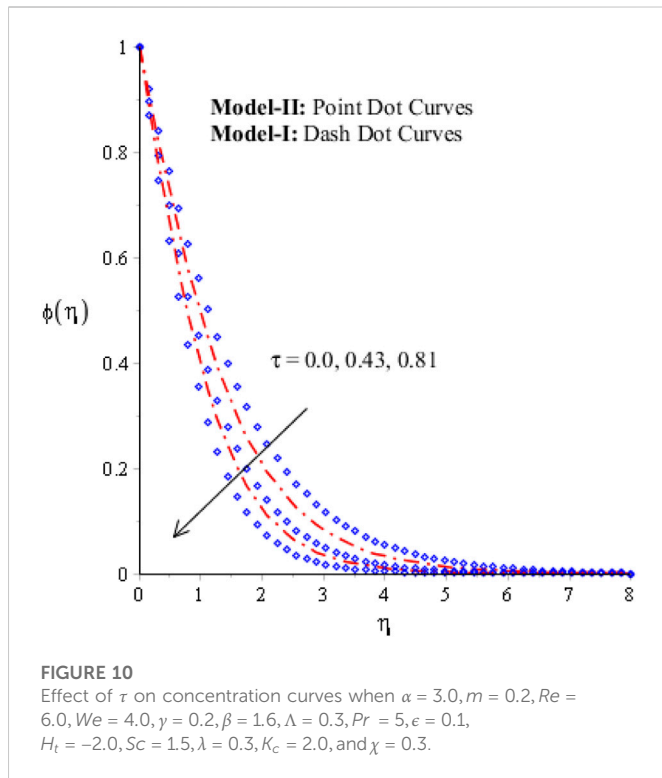
FIGURE 10
Effect of τ on concentration curves when $\alpha = 3.0, m = 0.2, Re = 6.0, We = 4.0, \gamma = 0.2, \beta = 1.6, \Lambda = 0.3, Pr = 5, \epsilon = 0.1, H_t = -2.0, Sc = 1.5, \lambda = 0.3, K_c = 2.0,$ and $\chi = 0.3.$

$$\frac{\left(\sum_{i=1}^{N}\left(\left|\omega^r - \omega^{r-1}\right|\right)^2\right)^{\frac{1}{2}}}{\left(\sum_{i=1}^{N}\left|\omega^r\right|\right)^2} < 10^{-8}. \tag{29}$$

Step-III: In this step, the system of linear equations is

$$M\left(F, N, \theta, \phi\right)\begin{bmatrix} F \\ \theta \\ \phi \end{bmatrix} = [F]. \tag{30}$$

Step-IV: Maple 18 was used to develop code regarding the FEM. The computational domain was taken as $[0, 8]$ and grid size study is

shown in Table 3. Validation of a present problem already published (Muhammad and Nadeem, 2017) is shown in Table 4.

4 Explanations regarding graphical outcomes

This study describes the development of a 2D model associated with mass diffusion and thermal energy in two viscosity models. Shape effects based on cylinder, platelet, brick, and sphere were assessed in mineral oil. Chemical reaction and heat generation/ absorption were also investigated. It is important to note that magnetic dipoles were taken out in this research project. Such considerations were used to generate a complex model, and the complex model was solved by implementing a finite element approach. Detailed outcomes based on graphical outcomes associated flow, mass diffusion, and thermal energy are discussed below.

4.1 Comparative impacts of viscosity models *via* flow distribution

The impacts of magnetic dipole number, heat source parameter, Weissenberg number, and Reynolds number on flow distribution were observed using model-I and model-II. These graphical outcomes are shown in Figures 2–4. Figure 2 demonstrates the distribution of We on flow distribution *via* two viscosity models. Flow is gradually slowed down *versus* variation in We. This decreasing impact is produced because of the concept of Weissenberg number. This concept involves the ratio between viscous and elastic forces. Here, We is a dimensionless number that is modeled using the concept of synovial fluid in the current model. In physics, division of elastic forces by viscous forces is called the Weissenberg number. An inverse proportional relation between We and a viscous force has been studied. Therefore, flow is reduced. Thickness associated with momentum layers is based on distribution in We. Viscous force is

TABLE 5 Numerical behavior of $We, H_t, \beta,$ and Sc on flow gradient, concentration gradient, and temperature gradient when $\alpha = 0.4, n = 0.2, Re = 2.0, \gamma = 0.2, \Lambda = 0.32, Pr = 5, \epsilon = 0.1, \lambda = 0.4, \gamma = 0.4, K_c = -1.5, \chi = 0.3,$ and $\tau = 0.3.$

Distribution in parameters		$-Re^{\frac{1}{2}}Cf$	$-Re^{-1/2}NU$	$-Re^{-1/2}Sh$
	0.0	0.1273,748,635	1.196,172,066	0.2713,624,327
We	0.6	0.2925,411,043	1.197,164,591	0.2713,245,446
	1.2	0.3592,454,952	1.197,715,853	0.2712,971,370
	−1.6	0.3572,115,843	0.8443,226,354	0.3274,391,887
H_t	0.4	0.3308,657,546	0.4674,461,360	0.2870,622,052
	0.8	0.3212,466,514	0.3573,940,886	0.2222,874,817
	0.0	0.3606,600,647	0.3746,374,058	0.2895,486,000
β	0.8	0.3617,286,068	0.2049,585,284	0.2387,259,550
	1.2	0.3637,933,627	0.1341,445,446	0.2179,434,740
	0.0	0.3535,361,988	0.3429,470,506	0.3490,419,026
Sc	0.6	0.3423,512,080	0.3426,948,032	0.4440,915,206
	1.4	0.3257,942,182	0.3423,634,404	0.5894,510,546

enhanced among momentum layers. Consequently, change in viscosity of motion can be determined by change in We. Flow for $We = 0$ is greater than flow for $We \neq 0$. Furthermore, thickness via momentum layers for model-I is greater than thickness via momentum layers for model-II. Figure 3 is plotted to measure the impact of H_t on flow distribution based on two viscosity models (model-II and model-I). It has been suggested that fluid particles absorb more heat energy when a heat source is applied. Two types of impacts are addressed when H_t is applied. One is heat generation via positive values and the other is heat absorption via negative values. This kind of impact occurs due to an external heat source. The flow produced using model-I is higher than the flow produced using model-II. Mathematically, H_t is proportional to the difference in temperature. Hence, heat variation is based on distribution in H_t. Velocity field is also based on distribution of heat energy. Motion of particles on the surface is enhanced when variation in heat is increased. Momentum thickness for $H_t < 0$ is greater than momentum thickness for $H_t > 0$. Thickness of thermal layers is an inclined function $versus$ heat source number. Moreover, flow for the case of model-I is greater than that for model-II. Different effects of magnetic dipole on flow behavior are associated with various shapes (Figure 4). From Figure 4, it is estimated that flow of nanoparticles declines with higher magnetic dipole number. β is a dimensionless number. The occurrence of β is due to a magnetic dipole at the wall (of the surface). A retardation force is visualized using the concept of magnetic dipole. Due to magnetic dipole, frictional force is also generated among layers (momentum) and flow slows due to frictional force. Furthermore, thickness (for momentum layers) is decreased when the strength of magnetic dipole is magnified. Velocity field for $\beta = 0$ is greater than velocity field for $\beta \neq 0$.

4.2 Comparative effects of viscosity models *via* thermal distribution

Figures 5–7 are plotted to estimate the effects of heat source number, Prandtl number, and magnetic dipole number on temperature profile. These figures indicate measurement of thermal distribution via model-I and model-II, which account for the impacts of nanoparticle shape. Figure 5 illustrates visualization of H_t on thermal field. Heat energy related to fluidic particles was improved using a heat source (external). Layers based on thermal boundary were enhanced against distribution in H_t. Hence, thermal energy can be adjusted using higher values of H_t. Mathematically, H_t appeared in the energy equation. From the energy equation, H_t has a proportional relation to temperature variation. Temperature is increased when H_t is distributed because of the direct proportional relation of $(T - T_\infty)$; H_t. Figure 5 shows two types of heat characterization. The mechanism of heat generation is based on $H_t > 0$, and the mechanism of heat absorption is based on $H_t < 0$. The thermal thickness (for thermal layers) for $H_t < 0$ is less than the thermal thickness for $H_t > 0$. In addition, thermal performance is boosted significantly in the case of model-I compared to the thermal energy in model-II. Figure 6 demonstrates the role of magnetic dipole (β) in thermal variation, showing that a magnetic dipole enhances heat energy in nanoparticles. Thermal layers have a tendency to absorb more heat energy when a magnetic dipole is

implemented. Mathematically, direct proportional relation between a magnetic dipole and temperature field has been visualized using the dimensionless energy equation. Consequently, an increase in β results in enhancement in the thermal field. Dimensionless parameter (β) brings enhancement in thickness of thermal layers. Furthermore, width of thermal layers for $\beta = 0$ is greater than width for $\beta > 0$. Hence, temperature of nanoparticles increased with an increase in magnetic dipole. Figure 7 predicts the impact of We on energy transfer. The thermal profile was inclined against implication of We. The formulation of We was modeled using tensor of synovial fluid in momentum equations. From a physics point of view, division between elastic force and viscous force is the Weissenberg number. By increasing the impact of We, the viscosity of particles is magnified when We is magnified. The width and thickness associated with thermal layers are magnified utilizing large values of We. Moreover, thickness of thermal layers for $We = 0$ is less than thickness of thermal layers for $We > 0$.

4.3 Comparative impacts of viscosity models *via* concentration distribution

Figures 8–10 show estimation of various important impacts of parameters on thermal energy that occurred in two viscosity models that account for impacts of nanoparticle shape. We demonstrate impacts of Sc, chemical reaction, and thermo-phoretic particle number on mass diffusion. The influence of Sc on concentration profile via two viscosity models is shown in Figure 8. Physically, diffusion into chemical species slowly declined when Sc was increased. The effects of Sc are modeled in the concentration equation. A division between viscous diffusion (rate) and mass diffusion (rate) is termed the Schmidt number. From this, Sc has an inverse proportional relation to mass species. Due to the inverse relation between Sc and mass diffusion, diffusion in mass species slows down. Furthermore, thickness via mass diffusion layers for $Sc = 0$ is higher than thickness via mass diffusion layers for $Sc \neq 0$. Mass diffusion in model-I is faster than mass diffusion in model-II. Figure 9 demonstrates the influence of chemical reaction number on concentration profile via two models of viscosity. In Figure 10, two types of chemical reactions are shown based on destructive chemical species and constructive chemical species in mass diffusion. In Figure 9, K_c is a dimensionless number that is utilized to assess chemical reaction toward a solute field. $K_c > 0$ is termed a destructive chemical (reaction), whereas the generative chemical (reaction) is dependent on $K_c < 0$, and $K_c = 0$ indicates that no chemical reaction has occurred. An enhancement in solute field occurs for the generative mechanism, but a decraese is observed on the solute field for destructive reaction (mechanism). Diffusion into chemical species slows down when chemical reaction into particles occurs. Furthermore, the amount of mass diffusion in model-II is less than the amount of mass diffusion in model-I. The thickness of concentration layers reduced with greater influence of chemical reaction number. Figure 10 demonstrates the effects of τ (thermophoretic parameter) on solute field via two viscosity models. Figure 10 indicates that the solute field decreases with enhancement in τ. Physically, this reduction happens because concentration decreases due to increased movement of particles.

4.4 Visualizations of mass diffusion rate, skin friction coefficient, and heat energy rate against different parameters

Impacts of $We, H_t, \beta,$ and Sc on mass diffusion rate, Nusselt number, and shear stress are shown in Table 5. Shear stress was reduced with greater influence of heat source number, but rates of mass diffusion and heat energy were enhanced with greater influence of H_t. Maximum amount of shear stress increases relative to distribution in magnetic dipole, and temperature and concentration gradients are reduced relative to the impact of magnetic dipole. Schmidt number increases mass diffusion rate. These outcomes are recorded in Table 5.

5 Conclusion

The numerical scheme, namely, finite element algorithm, has been applied successfully for the solution of heat and mass transportation in bio-fluids, implicating magnetic dipole in the effects of shape factors and nanoparticles. Important outcomes of the current study are:

➢ Velocity field increases relative to change in magnetic dipole and heat sink, but velocity field decreases with enhancement in We;
➢ The production for temperature field and mass diffusion for model-II is higher than that for mass diffusion and temperature field for model-I;
➢ Temperature gradient declines with enhancement in heat sink, magnetic dipole, and Weissenberg number, but opposite treatment was investigated in temperature field;
➢ An increment in $Sc, K_c,$ and τ decelerates solute field, while concentration gradient increases with enhancement in Sc;

➢ Maximum acceleration in velocity for model-I was greater than acceleration in velocity field for model-II.

Data availability statement

The raw data supporting the conclusions of this article will be made available by the authors, without undue reservation.

Author contributions

All authors listed have made a substantial, direct, and intellectual contribution to the work and approved it for publication.

Conflict of interest

The authors declare that the research was conducted in the absence of any commercial or financial relationships that could be construed as a potential conflict of interest.

Publisher's note

All claims expressed in this article are solely those of the authors and do not necessarily represent those of their affiliated organizations, or those of the publisher, the editors, and the reviewers. Any product that may be evaluated in this article, or claim that may be made by its manufacturer, is not guaranteed or endorsed by the publisher.

References

Akbar, N. S., Iqbal, Z., Ahmad, B., and Maraj, E. N. (2019). Mechanistic investigation for shape factor analysis of SiO2/MoS2–ethylene glycol inside a vertical channel influenced by oscillatory temperature gradient. *Can. J. Phys.* 97 (9), 950–958. doi:10.1139/cjp-2018-0717

Akbar, N. S., Maraj, E. N., Noor, N. F. M., and Habib, M. B. (2022). Exact solutions of an unsteady thermal conductive pressure driven peristaltic transport with temperature-dependent nanofluid viscosity. *Case Stud. Therm. Eng.* 35, 102124. doi:10.1016/j.csite.2022.102124

Akram, J., Akbar, N. S., Alansari, M., and Tripathi, D. (2022). Electroosmotically modulated peristaltic propulsion of TiO2/10W40 nanofluid in curved microchannel. *Int. Commun. Heat Mass Transf.* 136, 106208. doi:10.1016/j.icheatmasstransfer.2022.106208

Akram, J., Akbar, N. S., and Tripathi, D. (2021). A theoretical investigation on the heat transfer ability of water-based hybrid (Ag–Au) nanofluids and Ag nanofluids flow driven by electroosmotic pumping through a microchannel. *Arabian J. Sci. Eng.* 46 (3), 2911–2927. doi:10.1007/s13369-020-05265-0

Akram, J., Akbar, N. S., and Tripathi, D. (2022). Analysis of electroosmotic flow of silver-water nanofluid regulated by peristalsis using two different approaches for nanofluid. *J. Comput. Sci.* 62, 101696. doi:10.1016/j.jocs.2022.101696

Akram, J., Akbar, N. S., and Tripathi, D. (2022). Electroosmosis augmented MHD peristaltic transport of SWCNTs suspension in aqueous media. *J. Therm. Analysis Calorim.* 147 (3), 2509–2526. doi:10.1007/s10973-021-10562-3

Ali, U., Rehman, K. U., and Malik, M. Y. (2020). Thermal energy statistics for jeffery fluid flow regime: A generalized fourier's law outcomes. *Phys. A Stat. Mech. its Appl.* 542, 123428. doi:10.1016/j.physa.2019.123428

Babu, D. D., Venkateswarlu, S., and Keshava Reddy, E. (2020). Multivariate Jeffrey fluid flow past a vertical plate through porous medium. *J. Appl. Comput. Mech.* 6 (3), 605–616.

Choi, S. U., and Eastman, J. A. (1995). *Enhancing thermal conductivity of fluids with nanoparticles (No. ANL/MSD/CP-84938; CONF-951135-29)*. Lemont, Illinois: Argonne National Lab. ANL.

Gireesha, B. J., Umeshaiah, M., Prasannakumara, B. C., Shashikumar, N. S., and Archana, M. (2020). Impact of nonlinear thermal radiation on magnetohydrodynamic three dimensional boundary layer flow of Jeffrey nanofluid over a nonlinearly permeable stretching sheet. *Phys. A Stat. Mech. its Appl.* 549, 124051. doi:10.1016/j.physa.2019.124051

Gul, T., Khan, A., Bilal, M., Alreshidi, N. A., Mukhtar, S., Shah, Z., et al. (2020). Magnetic dipole impact on the hybrid nanofluid flow over an extending surface. *Sci. Rep.* 10 (1), 8474–8513. doi:10.1038/s41598-020-65298-1

Habib, M. B., and Akbar, N. S. (2021). New trends of nanofluids to combat *Staphylococcus aureus* in clinical isolates. *J. Therm. Analysis Calorim.* 143 (3), 1893–1899. doi:10.1007/s10973-020-09502-4

Hanif, H., and Shafie, S. (2022). Interaction of multi-walled carbon nanotubes in mineral oil based Maxwell nanofluid. *Sci. Rep.* 12 (1), 4712–4716. doi:10.1038/s41598-022-07958-y

Haroun, M. H. (2020). On electrohydrodynamic flow of Jeffrey fluid through a heating vibrating cylindrical tube with moving endoscope. *Archive Appl. Mech.* 90 (6), 1305–1315. doi:10.1007/s00419-020-01665-8

Hosseinzadeh, K., Asadi, A., Mogharrebi, A. R., Ermia Azari, M., and Ganji, D. D. (2021a). Investigation of mixture fluid suspended by hybrid nanoparticles over vertical cylinder by considering shape factor effect. *J. Therm. Analysis Calorim.* 143 (2), 1081–1095. doi:10.1007/s10973-020-09347-x

Hosseinzadeh, K., Moghaddam, M. E., Asadi, A., Mogharrebi, A. R., Jafari, B., Hasani, M. R., et al. (2021b). Effect of two different fins (longitudinal-tree like) and

hybrid nano-particles (MoS2-TiO2) on solidification process in triplex latent heat thermal energy storage system. *Alexandria Eng. J.* 60 (1), 1967–1979. doi:10.1016/j.aej.2020.12.001

Hosseinzadeh, K., Roghani, S., Mogharrebi, A. R., Asadi, A., Waqas, M., and Ganji, D. D. (2020). Investigation of cross-fluid flow containing motile gyrotactic microorganisms and nanoparticles over a three-dimensional cylinder. *Alexandria Eng. J.* 59 (5), 3297–3307. doi:10.1016/j.aej.2020.04.037

Hou, E., Jabbar, N., Nazir, U., Sohail, M., Javed, M. B., Shah, N. A., et al. (2022). Significant mechanism of Lorentz force in energy transfer phenomena involving viscous dissipation via numerical strategy.

Khan, M. I., Haq, F., Khan, S. A., Hayat, T., and Khan, M. I. (2020). Development of thixotropic nanomaterial in fluid flow with gyrotactic microorganisms, activation energy, mixed convection. *Comput. methods programs Biomed.* 187, 105186. doi:10.1016/j.cmpb.2019.105186

Khan, U., Zaib, A., Bakar, S. A., and Ishak, A. (2021). Stagnation-point flow of a hybrid nanoliquid over a non-isothermal stretching/shrinking sheet with characteristics of inertial and microstructure. *Case Stud. Therm. Eng.* 26, 101150. doi:10.1016/j.csite.2021.101150

Khan, U., Zaib, A., Ishak, A., Eldin, S. M., Alotaibi, A. M., Raizah, Z., et al. (2022). Features of hybridized AA7072 and AA7075 alloys nanomaterials with melting heat transfer past a movable cylinder with Thompson and Troian slip effect. *Arabian J. Chem.* 16, 104503. doi:10.1016/j.arabjc.2022.104503

Khan, U., Zaib, A., and Ishak, A. (2021). Magnetic field effect on Sisko fluid flow containing gold nanoparticles through a porous curved surface in the presence of radiation and partial slip. *Mathematics* 9 (9), 921. doi:10.3390/math9090921

Khan, U., Zaib, A., Ishak, A., Waini, I., Pop, I., Elattar, S., et al. (2022). Stagnation point flow of a water-based graphene-oxide over a stretching/shrinking sheet under an induced magnetic field with homogeneous-heterogeneous chemical reaction. *J. Magnetism Magnetic Mater.* 565, 170287. doi:10.1016/j.jmmm.2022.170287

Madhukesh, J. K., Varun Kumar, R. S., Punith Gowda, R. J., Prasannakumara, B. C., and Shehzad, S. A. (2022). Thermophoretic particle deposition and heat generation analysis of Newtonian nanofluid flow through magnetized Riga plate. *Heat. Transf.* 51 (4), 3082–3098. doi:10.1002/htj.22438

Manjunatha, G., Rajashekhar, C., Vaidya, H., Prasad, K. V., Makinde, O. D., and Viharika, J. U. (2020). Impact of variable transport properties and slip effects on MHD Jeffrey fluid flow through channel. *Arabian J. Sci. Eng.* 45 (1), 417–428. doi:10.1007/s13369-019-04266-y

Maraj, E. N., Akbar, N. S., Iqbal, Z., and Azhar, E. (2017). Framing the MHD mixed convective performance of CNTs in rotating vertical channel inspired by thermal deposition: Closed form solutions. *J. Mol. Liq.* 233, 334–343. doi:10.1016/j.molliq.2017.03.041

Maraj, E. N., Zehra, I., and SherAkbar, N. (2022). Rotatory flow of MHD (MoS2-SiO2)/H2O hybrid nanofluid in a vertical channel owing to velocity slip and thermal periodic conditions. *Colloids Surfaces A Physicochem. Eng. Aspects* 639, 128383. doi:10.1016/j.colsurfa.2022.128383

Muhammad, N., and Nadeem, S. (2017). Ferrite nanoparticles Ni-Zn Fe_2O_4, Mn-Zn Fe_2O_4 and Fe_2O_4 in the flow of ferromagnetic nanofluid. *Eur. Phys. J. Plus* 132 (9), 377–412. doi:10.1140/epjp/i2017-11650-2

Naseem, T., Nazir, U., Sohail, M., Alrabaiah, H., Sherif, E. S. M., and Park, C. (2021). Numerical exploration of thermal transport in water-based nanoparticles: A computational strategy. *Case Stud. Therm. Eng.* 27, 101334. doi:10.1016/j.csite.2021.101334

Rostami, A. K., Hosseinzadeh, K., and Ganji, D. D. (2022). Hydrothermal analysis of ethylene glycol nanofluid in a porous enclosure with complex snowflake shaped inner wall. *Waves Random Complex Media* 32 (1), 1–18. doi:10.1080/17455030.2020.1758358

Saif, R. S., Muhammad, T., Sadia, H., and Ellahi, R. (2020). Hydromagnetic flow of Jeffrey nanofluid due to a curved stretching surface. *Phys. A Stat. Mech. its Appl.* 551, 124060. doi:10.1016/j.physa.2019.124060

Salmi, A., Madkhali, H. A., Arif, U., Alharbi, S. O., and Malik, M. Y. (2022). Thermal bio-convective transport in biological fluid using two viscosity models. *Case Stud. Therm. Eng.* 34, 101924. doi:10.1016/j.csite.2022.101924

Shafee, A., Rezaeianjouybari, B., and Tlili, I. (2021). Treatment of nanofluid within porous media using non-equilibrium approach. *J. Therm. Analysis Calorim.* 144 (4), 1571–1583. doi:10.1007/s10973-020-09587-x

Shehzad, S. A., Reddy, M. G., Rauf, A., and Abbas, Z. (2020). Bioconvection of Maxwell nanofluid under the influence of double diffusive Cattaneo–Christov theories over isolated rotating disk. *Phys. Scr.* 95 (4), 045207. doi:10.1088/1402-4896/ab5ca7

Sinha, V. K., Kumar, B., Seth, G. S., and Nandkeolyar, R. (2020). Features of Jeffrey fluid flow with Hall current: A spectral simulation. *Pramana* 94 (1), 64–68. doi:10.1007/s12043-020-1940-y

Sohail, M., El-Zahar, E. R., Mousa, A. A. A., Nazir, U., Althobaiti, S., Althobaiti, A., et al. (2022a). Finite element analysis for ternary hybrid nanoparticles on thermal enhancement in pseudo-plastic liquid through porous stretching sheet. *Sci. Rep.* 12 (1), 9219–9313. doi:10.1038/s41598-022-12857-3

Sohail, M., Nazir, U., El-Zahar, E. R., Alrabaiah, H., Kumam, P., Mousa, A. A. A., et al. (2022b). A study of triple-mass diffusion species and energy transfer in Carreau–Yasuda material influenced by activation energy and heat source. *Sci. Rep.* 12 (1), 10219–10317. doi:10.1038/s41598-022-13890-y

Veera Krishna, M. (2020). Heat transport on steady MHD flow of copper and alumina nanofluids past a stretching porous surface. *Heat. Transf.* 49 (3), 1374–1385. doi:10.1002/htj.21667

Wang, F., Sohail, M., Nazir, U., El-Zahar, E. R., Park, C., and Jabbar, N. (2022). An implication of magnetic dipole in Carreau Yasuda liquid influenced by engine oil using ternary hybrid nanomaterial. *Nanotechnol. Rev.* 11 (1), 1620–1632. doi:10.1515/ntrev-2022-0100

Waqas, H., Khan, S. U., Bhatti, M. M., and Imran, M. (2020). Significance of bioconvection in chemical reactive flow of magnetized Carreau–Yasuda nanofluid with thermal radiation and second-order slip. *J. Therm. Analysis Calorim.* 140 (3), 1293–1306. doi:10.1007/s10973-020-09462-9

Nomenclature

v, u Velocity components (ms^{-1})

ρ Density (Kgm^{-3})

H Magnetic field (tesla)

μ_0 Dynamic viscosity at zero $(Kgm^{-1}s^{-1})$

n Power-law index number

α Concentration-dependent viscosity number

C_p Specific heat capacity $(JKg^{-1}K)$

Q_0 Heat generation

C_∞ Ambient concentration (s^{-1})

PDEs Partial differential equations

U_w Wall velocity (ms^{-1})

δ Region of a magnetic dipole

θ Dimensionless temperature

Re Reynolds number

ν Kinematic viscosity (m^2s^{-1})

H_t Heat source parameter

Sc Schmidt number

ϵ Material parameter

Sh Schmidt number

ψ_j Stream function

N Deformation tensor

T_c Highest temperature rather than wall temperature

τ Thermophoretic parameter

T_s Reference temperature (K)

N_f Nanofluid

Y, X Space coordinates (m)

P Pressure (Nm^{-2})

M Magnetization number

μ Viscosity $(Kgm^{-1}s^{-1})$

γ *Material* parameter

ϕ Concentration

T Fluidic temperature (K)

T_∞ Ambient temperature (K)

K Thermal conductivity (Wm^{-1})

C Concentration (s^{-1})

T_w Wall temperature (K)

β Hydrodynamic interaction number

F Dimensionless velocity

η Independent variable

we Weissenberg number

Pr Prandtl number

K_c Chemical reaction number

NU Nusselt number

ODEs Ordinary differential equations

FEM Finite element method

b, ε Material parameters

D Mass diffusion (m^2s^{-1})

χ Volume fraction of nanoparticles

k_{ν_f} Thermophoretic constant

ODEs Ordinary differential equations